

Long-Period Ground Motion Simulation Based on Three-dimensional Centroid Moment Tensor Inversion Solutions in the Kanto Region, Japan

Shunsuke Takemura (✉ shunsuke@eri.u-tokyo.ac.jp)

Earthquake Research Institute, the University of Tokyo <https://orcid.org/0000-0002-7511-3443>

Kazuo Yoshimoto

Yokohama City University

Katsuhiro Shiomi

National Research Institute for Earth Science and Disaster Resilience

Full paper

Keywords: CMT inversion, Kanto region, Long-period ground motion, 3D numerical simulation

Posted Date: July 20th, 2020

DOI: <https://doi.org/10.21203/rs.3.rs-43689/v1>

License:  This work is licensed under a Creative Commons Attribution 4.0 International License.

[Read Full License](#)

Version of Record: A version of this preprint was published on January 11th, 2021. See the published version at <https://doi.org/10.1186/s40623-020-01348-2>.

Abstract

We conducted centroid moment tensor (CMT) inversions of moderate (M_w 4.5–6.5) earthquakes in the Kanto region, Japan, using a local three-dimensional (3D) model. We then investigated the effects of our 3D CMT solutions on long-period ground motion simulations. Grid search CMT inversions were conducted using displacement seismograms for periods of 25–100 s. By comparing our 3D CMT solutions with those from the local one-dimensional (1D) catalog, we found that our 3D CMT inversion systematically provides magnitudes smaller than those in the 1D catalog. The M_w differences between 3D and 1D catalogs tend to be significant for earthquakes within the oceanic slab. By comparing ground motion simulations between 1D and 3D velocity models, we confirmed that observed M_w differences could be explained by differences in the rigidity structures around the source regions between 3D and 1D velocity models. The 3D velocity structures (especially oceanic crust and mantle) are important for estimating seismic moments in intraslab earthquakes. The seismic moments directly affect the amplitudes of ground motions. Thus, 3D CMT solutions are essential for the precise forward and inverse modeling of long-period ground motion. We also conducted long-period ground motion simulations using our 3D CMT solutions to evaluate reproducibility of long-period ground motions at stations within the Kanto Basin. The simulations of our 3D CMT inversion well-reproduced observed ground motions for periods longer than 10 s, even at stations within the Kanto Basin.

Introduction

Long-period ground motions with predominant periods of several to 20 s have often been observed in large sedimentary basins and offshore regions. The duration and amplitude of long-period ground motion is enhanced due to thick low-velocity sediments along the propagation path (e.g., Boore 1999; Furumura et al. 2001, 2008; Olsen et al. 2006; Day et al. 2008; Gomberg 2018; Kaneko et al. 2019). Thus, long-period ground motions can cause severe resonance and damage of large-scale man-made structures, such as high-rise buildings, oil storage tanks, and suspension bridges. The characteristics of long-period ground motions were have been summarized in Koketsu and Miyake (2008). In the Kanto region, Japan, long-period ground motions with predominant periods of 5–10 s have frequently been observed during shallow moderate-to-large earthquakes (e.g., Kinoshita et al. 1992; Miyake and Koketsu 2005; Yoshimoto and Takemura 2014). The propagation feature of long-period ground motion is complicated due to the lateral variations of sedimentary structures within the Kanto Basin (e.g., Koketsu and Kikuchi 2000; Furumura and Hayakawa 2007; Mukai et al. 2018). Long-period ground motion and the structural properties within the Kanto Basin have been studied extensively using observed seismograms and geological surveys to contribute to disaster mitigation in the Tokyo metropolitan area (e.g., Koketsu et al. 2009; Takemura et al. 2015).

Recent advances in numerical simulation codes (e.g., Gokhberg and Fichtner 2016; Maeda et al. 2017) and local/regional three-dimensional (3D) velocity structure models (e.g., Koketsu et al. 2012; Kennett et al. 2013; Stephenson et al. 2017) have enabled the implementation of realistic 3D simulations of long-period ground motion (e.g., Komatitsch 2004; Iwaki et al. 2018; Wirth et al. 2019), and the estimation of

structural properties (e.g., Tape et al. 2009; Gao and Shen 2014; Miyoshi et al. 2017). In forward and inverse modeling of long-period ground motion and structural properties along propagation paths, an assumption of a double-couple point source is usually assumed. The centroid moment tensor (CMT) solutions based on displacement for periods longer than 20 s are generally considered robust against structural heterogeneities, compared to first-motion solutions (e.g., Takemura et al. 2016). As such, one-dimensional (1D) velocity models are adopted in local/global CMT inversion systems (e.g., Kubo et al. 2002; Bernardi et al. 2004; Vallée et al. 2011; Ekström et al. 2012); these solutions are typically used in ground motion simulations. However, in regions with strong heterogeneities, such as thick sediments and subducting oceanic plates, focal mechanisms could be incorrectly estimated using conventional 1D CMT methods. To address this issue, the CMT inversion based on Green's functions using the local/regional 3D model has been developed in such regions (e.g., Lee et al. 2013; Hejrani et al. 2017; Okamoto et al. 2018; Takemura et al. 2018b, a, 2019b, 2020; Wang and Zhan 2020; Hejrani and Tkalcic 2020). By using the 3D CMT results of moderate earthquakes along the Nankai Trough, Takemura et al. (2020) demonstrated that the differences in centroid depths and focal mechanisms between 1D and their 3D CMT solutions were significant for offshore earthquakes due to offshore heterogeneities. These differences could affect ground motion simulations (e.g., Takemura et al. 2019c). To achieve precise forward and inverse modeling of long-period ground motions in the Kanto region, where large sedimentary basin and two subducting plates exist, accurate CMT solutions should be required.

In this study, we conduct CMT inversions of moderate earthquakes in the Kanto region using the 3D Green's function dataset. We evaluate differences in source parameters between 1D and 3D CMT solutions. We conduct ground motion simulations using 3D CMT solutions to discuss the effects of CMT solutions on long-period ground motion modeling in the Kanto Basin. To accurately model phases and amplitudes of long-period ground motion, we demonstrate that the adjusted source model should be incorporated in the used 3D model (e.g., 3D CMT solution).

Method

In this study, we used the F-net broadband seismograms of the target earthquakes. At each F-net station (filled triangles in Fig. 1), a broadband velocity seismometer (STS-1, STS-2, or STS-2.5) was installed. The health of sensors has been systematically monitored by the National Research Institute for Earth Science and Disaster Resilience (NIED; Okada et al. 2004; Kimura et al. 2015; National Research Institute for Earth Science and Disaster Resilience 2019). Our target earthquakes were shallow (≤ 50 km) earthquakes with moment magnitudes (M_w) between 4.5–6.5, listed in the F-net moment tensor (MT) catalog. The F-net 1 D velocity structure model has been used in the F-net MT catalog (Fukuyama et al. 1998; Kubo et al. 2002). Target earthquakes (focal mechanisms in Fig. 1) occurred within the area of assumed source grids (crosses in Fig. 2a) between April 2017 and March 2020. The data of the Metropolitan Seismic Observation Network (MeSO-net) was also available from the NIED website in the analyzed period (e.g., Kasahara et al. 2009; Sakai and Hirata 2009). As MeSO-net stations were densely deployed around the Tokyo metropolitan area in Japan (inverse triangles in Fig. 1), we also evaluated long-period ground motion in the Kanto Basin using earthquakes that occurred after April 2017.

CMT inversions were conducted using displacement seismograms for periods of 25–100 s. By using the Open-source Seismic Wave Propagation Code software (OpenSWPC; Maeda et al. 2017), we numerically evaluated Green's functions in the 3D model. We used the Japan Integrated Velocity Structure Model version 1 (JIVSM; Koketsu et al. 2012) as the 3D velocity structure model for this study. The JIVSM has been widely used in the evaluation of ground motion, crustal deformation, and seismic monitoring across Japan (e.g., Guo et al. 2016; Miyazawa 2016; Agata 2020; Oba et al. 2020; Baba et al. 2020). The simulation model covered an area of $600 \times 600 \times 160$ km³ (blue dashed rectangle in Fig. 2a), which was discretized by grid intervals of 0.5 km in the horizontal direction and 0.2 km in the vertical direction. The physical parameters of each layer in the JIVSM are listed in Table 1. The minimum S-wave velocity was assumed to be 1.5 km/s for the calculation of 3D Green's functions. Source grids were uniformly distributed at a horizontal interval of 0.1° at 6 to 60 km depths, with an interval of 2 km. The “Seismic Analysis Code” (SAC; Goldstein and Snoke 2005; Helffrich et al. 2013) was used to store simulated seismograms and conduct a part of signal processing. Approximately 13 000 000 Green's function SAC files from 49 279 source grids to 15 F-net stations were obtained by conducting 45 reciprocal calculations. Each reciprocal calculation required 247 GB of computer memory and a wall-clock time of 1 h by parallel computing with 432 cores of the computer system of Earthquake and Volcano Information Center at the Earthquake Research Institute, the University of Tokyo.

Table 1

Physical parameters of each layer in JIVSM. The air and seawater layers were treated as being the same, following Maeda et al. (2017). The *P*-wave velocity (V_P), *S*-wave velocity (V_S), density (ρ), rigidity (μ) and inelastic attenuation (Q_P and Q_S) are listed.

	V_P [km/s]	V_S [km/s]	ρ [kg/m ³]	μ [GPa]	Q_P	Q_S
Air	0.0	0.0	0.001	0.0	10^{10}	10^{10}
seawater	1.5	0.0	1.04	0.0	10^6	10^6
Sedimentary layer 1	1.8	0.5	1.95	0.49	170	100
Sedimentary layer 3	2.3	0.9	2.10	1.70	340	200
Sedimentary layer 4	3.0	1.5	2.25	5.06	510	300
Basement	5.5	3.2	2.65	27.1	680	400
Upper crust	5.8	3.4	2.70	31.2	680	400
Lower crust	6.4	3.8	2.80	40.0	680	400
Upper mantle	7.5	4.5	3.20	64.8	850	500
Philippine Sea plate						
Oceanic crust layer 2	5.0	2.9	2.40	20.2	340	200
Oceanic crust layer 3	6.8	4.0	2.90	46.4	510	300
Oceanic Mantle	8.0	4.7	3.20	70.7	850	500
Pacific Plate						
Oceanic crust layer 2	5.4	2.8	2.60	20.4	340	200
Oceanic crust layer 3	6.5	3.5	2.80	34.3	510	300
Oceanic Mantle	8.1	4.6	3.40	71.9	850	500

We choose F-net stations within epicentral distances between 100–400 km from the initial epicenter, obtained from the F-net MT catalog. A set of Green's functions at the source grids, which were located in $\pm 0.4^\circ$ grids from the initial epicenter and distributed at depths between 6–60 km, were selected for grid search inversion. A 200 s time window for each CMT inversion at every 1 s was adopted to determine the

centroid time. Time shifts were not permitted during grid search inversion, despite typical 1D MT routines such as the F-net MT system, enabling time shifts at each station between synthetic and observed seismograms. After CMT inversions, we obtained seismic moments and focal mechanisms at all times and selected source grids. Then, we evaluated variance reductions (VRs) between the observed and synthetic displacement seismograms for periods of 25–100 s. If there was a perfect match between the observed and synthetic seismograms, the VR is 100%. The maximum VR solution was considered the optimal solution, providing the optimal centroid location, depth, time, focal mechanism, and seismic moment. Other technical details of 3D CMT inversions and the evaluation of Green's functions are described in Takemura et al. (2020).

We conducted forward simulations of ground motion in the Kanto region to investigate the effects of CMT solutions on long-period (> 5 s) ground motion using 3D CMT solutions. A more realistic velocity model, including lower ($V_S < 1.5$ km/s) velocity layers, should be used in simulations of long-period ground motion. As such, the model in long-period ground motion simulations included all sedimentary layers of the JIVSM listed in Table 3. The model covered an area of $480 \times 480 \times 100$ km³ (red dotted rectangle in Fig. 2a), which was discretized by grid intervals of 0.2 km in the horizontal direction and 0.1 km in the vertical direction. Simulated seismograms were evaluated at the F-net and MeSO-net stations within the calculation region (red dotted rectangle in Fig. 2a). The source parameters for events a, b, and A–C are listed in Table 3. The 3D CMT solutions of the centroid locations, times, and moment tensors were used for the listed earthquakes. The source time functions were characterized by the Küpper wavelet, and durations were determined by the empirical relationship between seismic moments and rupture durations (Kanamori and Brodsky 2004). Each simulation of long-period ground motion required 1190 GB of computer memory and a wall-clock time of 4 h; simulations were performed by parallel computing with 64 nodes of the Fujitsu PRIMERGY CX600M1/CX1640M1 (Oakforest-PAC) in the Information Technology Center, University of Tokyo.

Table 3

Source parameters of long-period ground motions. Origin times of events a, b, A, B, and C were 10:02:45 JST on November 17, 2017, 19:56:05 JST on August 6, 2018, 19:23:01 JST on August 4, 2019, 03:23:54 JST on January 3, 2020, and 20:19:56 JST on February 6, 2020, respectively.

Source durations were assumed using the empirical relationship between seismic moments and durations (Kanamori and Brodsky 2004).

Lon. [°]	Lat. [°]	Depth [km]							Exp.	Dur. [s]	
			m_{rr}	$m_{\theta\theta}$	$m_{\varphi\varphi}$	$m_{r\theta}$	$m_{r\varphi}$	$m_{\varphi\theta}$			
a	141.4	37.2	44	3.365	-0.118	-1.848	1.191	3.131	-0.649	22	1
b	141.0	35.6	32	2.659	0.623	2.077	-0.707	3.068	-1.249	22	1
A	141.9	37.6	56	2.540	-0.520	-2.144	1.004	2.352	-1.102	25	5
B	141.1	36.0	36	1.128	-0.696	-0.711	0.055	2.408	-0.210	24	3
C	141.8	36.4	8	-1.402	-0.082	0.713	-0.239	1.316	-0.043	24	2

Results

3d Cmt Solutions Of Moderate Earthquakes Beneath Kanto Region

Figures 2b–d show an example of the 3D CMT inversion. The optimal solution for an earthquake on June 8, 2017 is a low-angle (22°) thrust faulting at a depth of 48 km, close to the upper surface of the Pacific Plate. The F-net MT solution of this earthquake was also a similar focal mechanism; however, its centroid depth was slightly deeper than that of our solution. The spatial variation of the VRs at each source grid is illustrated in Fig. 2c. Although the optimal depth was very close to the upper surface of the Pacific Plate, high (> 80%) VR solutions appeared at a wider depth range (36–56 km). These features are similar to CMT solutions in the Hyuga-nada region, southwest Japan (Fig. 4 of Takemura et al. 2020). The synthetic seismograms of the optimal solution accurately reproduce the observations.

We obtained 74 CMT solutions for shallow earthquakes (< 50 km) with an Mw of 4.2–6.3; Fig. 3a illustrates the spatial distribution of these CMT solutions. All parameters for these CMT solutions are available from the data repository site (<https://doi.org/10.5281/zenodo.3926884>). While the centroid times are essentially described in Japan Standard Time (JST), the comma-separated values file for the catalog also provides this in the Coordinated Universal Time (UTC) format.

Cross-sections of profiles A and B are also plotted at the bottom of Fig. 3a. Along with profile B, many earthquakes occurred just below the upper surface of the Pacific Plate. This seismicity was also confirmed in the hypocenter distribution determined by temporal ocean bottom seismometers (Ito et al. 2017b, a). However, these aligned intraslab earthquakes were not confirmed in the F-net catalog (Fig. 3b). As such, although the resolution of centroid depth is not very high, the 3D CMT inversion is also considered to work well in the Kanto region.

Differences between 3D CMT and F-net MT catalogs

The F-net solutions of corresponding earthquakes are also plotted in Fig. 3b. Spatial distributions of both catalogs seem to be similar. To quantitatively evaluate differences between the 3D CMT in this study and the F-net MT catalogs, we calculated cross-correlation coefficients of P -wave radiation patterns (e.g., Kuge and Kawakatsu 1993; Helffrich 1997), depth, and Mw differences between the 3D CMT and F-net MT catalogs (Fig. 4). A large negative value (-0.6) of cross-correlation coefficients only appeared in a solution for an earthquake on February 23, 2019. Only 4 F-net stations (N.JIZF, N.KZKF, N.YMZF, and N.KSKF; see Fig. 2b) were applicable for the CMT inversion of this earthquake because of the signal-to-noise ratio (SNR) for 25–100 s periods. Additionally, the VR of the 3D CMT solution was not high (~ 57%).

With the exception of this event, differences in focal mechanisms and centroid depths were not significant compared to offshore earthquakes along the Nankai Trough (Fig. 8 of Takemura et al. 2020).

On the other hand, we found that the M_w values based on the 3D CMT were systematically smaller than those of the F-net MT catalog (Fig. 4c). The M_w values are very important for ground motion simulations because values of seismic moments are directly related to the amplitude of the simulated ground motion. Using the 3D CMT catalog along the Nankai Trough (Takemura et al. 2020; <https://doi.org/10.5281/zenodo.3674161>), we also evaluated the differences in the M_w between 3D CMT and F-net MT solutions. We found both larger and smaller M_w values compared to the F-net catalog in the Nankai region (Fig. 5). In the Kanto and Nankai regions, the differences in M_w for offshore earthquakes were larger than those of onshore earthquakes; these differences may be caused by 3D heterogeneities.

To investigate the cause of these M_w differences, we conducted ground motion simulations for earthquakes on November 17, 2017 (Event a) and August 4, 2018 (Event b). Using the 3D CMT method, Events a and b were located just below the upper surface of the oceanic crust layer 2 and the boundary between oceanic crust layers 2 and 3 of the Pacific Plate, respectively. The M_w differences for events a and b were -0.31 and -0.25, respectively, and the estimated seismic moments of the 3D CMT solutions were approximately 35% and 42% of the F-net 1D solutions, respectively. We conducted simulations using the same source models and three different heterogeneous models; the JIVSM (Koketsu et al. 2012), the JIVSM without sediments, and the F-net 1D model (Kubo et al. 2002). The source models were the optimal solutions of 3D CMT inversion for two earthquakes (Events a and b in Table 3).

Figure 6 compares the simulated and observed vertical velocity seismograms. Two F-net stations were selected, and other simulation results were stored at <https://doi.org/10.5281/zenodo.3926888>. We found that simulation results using the JIVSM and the JIVSM without sediments reproduced observed F-net seismograms, with the exception of the N.JIZF seismograms for the JIVSM without sediments. This suggests that the effects of low-velocity sediments around the Kanto region on CMT inversion using long-period (25–100 s) seismograms are minor. Because the Kanto Basin and marine sediments exist along the path from event b to N.JIZF, the difference in waveforms of N.JIZF for periods of 10–50 s might appear. Around the Nankai Trough, a thicker (> 5 km) accretionary prism has a significant influence on surface waves even for periods longer than 20 s, and consequently the affects results of CMT inversions and ground motion simulations (e.g., Nakamura et al. 2015; Takemura et al. 2018b, a, 2019a, b, 2020).

On the other hand, the amplitudes of simulation seismograms with a similar source and the F-net 1D model were approximately 35–45% of the observed amplitudes. The effects of the Kanto Basin have a

minor influence on ground motion at outcrop rock sites (F-net), and differences in mechanisms and depths compared with F-net solutions that are not significant. This difference could be explained by differences in heterogeneities around the seismic source. The 3D CMT solutions of events a and b were located just beneath the upper surface of the oceanic crust layer 2 and near the boundary between oceanic crust layers 2 and 3 of the Pacific Plate, respectively. In the JIVSM (Table 1), the rigidities of source areas for both events were 20.4–34.3. In contrast, the rigidity at depths between 33–100 km was a uniform value (63.7 GPa; Table 2) in the F-net 1D model. The differences in rigidities around source regions between the JIVSM and the F-net 1D model correspond to differences in seismic moments between the 3D CMT and F-net MT solutions (34–42%). As such, it may be concluded that the major cause of differences in seismic moments between the 3D CMT and F-net 1D MT solutions is the difference in rigidity around the source areas.

Table 2
F-net 1D velocity model. The physical parameters were referred from Kubo et al. (2002).

Thickness (Depth) [km]	V_P [km/s]	V_S [km/s]	ρ [kg/m ³]	μ [GPa]	Q_P	Q_S
3 (0–3)	5.5	3.14	2.3	22.7	600	300
15 (3–18)	6.0	3.55	2.4	30.2	600	300
15 (18–33)	6.7	3.83	2.8	41.1	600	300
67 (33–100)	7.8	4.46	3.2	63.7	600	300
125 (100–225)	8.0	4.57	3.3	67.7	600	300
100 (225–325)	8.4	4.80	3.4	78.3	600	300
100 (325–425)	8.6	4.91	3.5	84.4	600	300
–	9.3	5.31	3.7	104	600	300

For the Nankai Trough, both overestimations and underestimations of seismic moments compared to the F-net catalog were observed (Fig. 5). Large M_w differences only appeared in the offshore region, where many intraslab and interplate earthquakes occurred. In particular, intraslab earthquakes along the Nankai Trough occurred within the low-velocity oceanic crust and high-velocity oceanic mantle (see Figs. 5 and 6 of Takemura et al. 2020), not modeled in the F-net 1D model. The difference in M_w values along the Nankai Trough could also be explained by the differences in heterogeneous structures between the 3D and 1D models.

In the F-net routine system, the origin times and epicenters were fixed as those in the JMA unified hypocenter catalog, and time shifts between observed and synthetic seismograms at each station were enabled. Miyoshi et al. (2017) notes that prior to estimating structural properties, the re-evaluation of centroid times for F-net MT solutions should be required to obtain suitable waveform inversion results. In

this study, we found that the estimation of seismic moments was affected by the rigidity structure around the source region. The difference in the estimation of seismic moments directly impacts the amplitude of ground motion simulations. The amplitude of ground motion simulation is important to evaluate seismic hazards and estimate structural properties along propagation paths. For 3D forward and inverse modeling of seismic ground motion, the adjusted source model observed and synthetic seismograms in the assumed local 3D model should be used, such as the 3D CMT solution.

Long-period ground motion simulations in the Kanto region

By using our the 3D CMT solutions based on the JIVSM, we conducted numerical simulations of long-period ground motions and compared with the observed seismograms. For the SNR of the MeSO-net for periods longer than 5 s, three earthquakes were selected with an M_w equal to or larger than 5.5 for simulations of long-period ground motion in the Kanto Basin. The source parameters of selected events (A–C) are listed in Table 3. Complete files of simulated velocity waveforms and wavefields are available online <https://doi.org/10.5281/zenodo.3926888>.

Figure 7 shows an example of simulated vertical velocity wavefields for the simulation of Event A at 40, 60, 80, 100, 120, 140, 160, and 180 s from the earthquake origin (movie file is also available from <https://doi.org/10.5281/zenodo.3926888>). The seismic waves radiated from the source complicatedly propagate through the Kanto region. In the Kanto, Niigata, and offshore regions, the wavelengths and propagation speeds of the Rayleigh waves became shorter and slower due to low-velocity sediments. The energy of these shorter-wavelength components (i.e., long-period ground motion) was trapped within low-velocity sediments. Thus, the duration of long-period ground motion was elongated in the Kanto, Niigata, and offshore regions (lapse time of 180 s). Peak ground velocities (PGVs) were calculated by the vector sum of three-component filtered seismograms at the F-net and MeSO-net stations; the passband period was 5–30 s. Figure 8 shows the spatial distributions of PGVs for each event. With the exception of Event C, the simulations were able to roughly reproduce the observed features of PGVs. Large PGVs appeared in regions with bedrock depths greater than 3 km.

Figures 9, 10, and 11 compare the filtered seismograms (15–30, 10–20, and 5–16 s) between observations and simulations. We selected two F-net stations and three MeSO-net stations. The selected MeSO-net stations are located at the site with deeper (> 3 km) bedrock depths. Simulations reproduced the observed seismograms at two F-net stations (N.ASIF and N.JIZF), with the exception of the simulation results for Event C for periods of 5–16 s. These results suggest that these 3D CMT solutions have the ability to reproduce observed ground motion with sufficient accuracy for periods longer than 5 s at F-net stations, which are deployed at outcrop rock sites. Although the observed seismograms at MeSO-net stations were reproduced by the simulated seismograms for periods longer than 10 s with the exception of the later phases at E.YROM, the simulation results for 5–16 s periods could not explain the observed seismograms in the Kanto Basin. These seismogram discrepancies at the MeSO-net stations could be caused by the JIVSM sedimentary structure. For Event C, because the centroid depth was 8 km, the

ground motion for 10–20 and 5–16 s periods were affected by the Kanto sedimentary basin oceanic sediments from the epicenter to coastal regions. Thus, these sedimentary structures in the offshore region may decrease waveform fitness for this event. The overestimation of PGVs (Fig. 8c) may also be attributed to the models of the Kanto Basin and the oceanic sediments along propagation paths.

Conclusions

We conducted CMT inversions of moderate earthquakes in the Kanto region from April 2017 to March 2020. The estimated focal mechanisms and depths using the 3D CMT method were not significantly different from the corresponding F-net MT solutions. However, the M_w values were systematically smaller than those in the F-net catalog. Earthquakes with large M_w differences tended to be located within the subducting plate, i.e., intraslab earthquakes. Using numerical simulations with 3D and 1D velocity models, we concluded that the major cause for the M_w differences is the difference in rigidity between the 1D and 3D velocity models. The 3D subducting oceanic crust and mantle could not be modeled in the 1D CMT system. The differences in the estimation of seismic moments directly affect the amplitude of ground motion simulations. The 3D simulation of an intraslab earthquake using the 1D CMT catalog could cause overestimations in the amplitude, even at outcrop rock sites. The 3D CMT solutions should be adopted for precise forward and inverse modeling of long-period ground motion simulations.

Simulations using the 3D CMT solutions in this study and the JIVSM were able to reproduce ground motion for periods longer than 5 s at outcrop rock sites. This means that the 3D CMT inversion works well in the Kanto region, and 3D CMT solutions are suitable for modeling long-period (> 5 s) ground motion. However, while simulations at stations within the Kanto Basin reproduced observed seismograms for periods longer than 10 s, the reproducibility of these simulations decreased for periods shorter than 10 s.

In the Kanto region, because the predominant period of long-period ground motion is approximately 6 s, a well-constrained sedimentary model is required to evaluate long-period ground motion for observed and anticipated large earthquakes. Recently, other regional/local velocity structure models of the sedimentary basin and subducting oceanic plate have been released (e.g., Hirose et al. 2008; Takemura et al. 2015; Headquarters for Earthquake Research Promotion 2017; Ito et al. 2019). The reproducibility of long-period ground motion in the Kanto Basin can improve through the utilization of other published or adjusted models based on ground motion simulations using 3D CMT solutions; this should be the primary focus of future research.

Declarations

Abbreviations

1D	
one-dimensional	
3D	
three-dimensional	
CMT	
centroid moment tensor	
ERI-JURP	Earthquake Research Institute, the University of Tokyo Joint Usage/Research Program
F-net	
Full-range seismograph network	
JIVSM	
Japan Integrated Velocity Structure Model version 1	
JST	
Japan Standard Time	
MeSO-net	
Metropolitan Seismic Observation network	
MT	
moment tensor	
NIED	
National Research Institute for Earth Science and Disaster Resilience	
OpenSWPC	
Open-Source Seismic Wave Propagation Code	
SAC	
Seismic Analysis Code	
SNR	
Signal to noise	
UTC	
Coordinated Universal Time	
VR	
Variance Reduction	

Declarations

Ethics approval and consent to participate

Not applicable.

Consent for publication

Not applicable.

Competing interests

The authors declare that they have no competing interests.

Availability of data and materials

By using HinetPy (<https://doi.org/10.5281/zenodo.3695076>), NIED F-net and MeSO-net data were downloaded from <https://hinetwww11.bosai.go.jp/auth/?LANG=en>. We used the open-source code OpenSWPC version 5.0.2 (<https://doi.org/10.5281/zenodo.3712650>) and the local 3D model “JIVSM” by Koketsu et al. (2012) from

https://www.jishin.go.jp/evaluation/seismic_hazard_map/lphm/12_choshuki_dat/. Figure images were drawn using Generic Mapping Tools (Wessel et al. 2013) and the Seismic Analysis Code (Goldstein and Snoke 2005; Helffrich et al. 2013) was used in a part of signal processing works. The CMT solutions in Takemura et al. (2020) and this study are available from <https://doi.org/10.5281/zenodo.3674161> and <https://doi.org/10.5281/zenodo.3926884>, respectively. Simulation results for long-period ground motion are also available at <https://doi.org/10.5281/zenodo.3926888>.

Funding

This study was supported by the JSPS KAKENHI grant number 19H04626 in Scientific Research on Innovative Areas “Science of slow earthquakes” This study was also supported by the ERI JURP 2020-S-04.

Authors' contributions

ST conducted a numerical simulation to synthesize Green’s functions and long-period ground motion, CMT inversions of moderate size earthquakes in the Kanto region, and also drafted this manuscript. ST and KY investigated propagation features of long-period ground motions. ST and KS interpreted the local seismicity beneath the Kanto region. All authors have read and approved the final manuscript.

Acknowledgements

Numerical simulations of seismic wave propagation were conducted using the computer system of Earthquake and Volcano Information Center at the Earthquake Research Institute, the University of Tokyo, and Fujitsu PRIMERGY CX600M1/CX1640M1 (Oakforest-PAC) at the Information Technology Center, the University of Tokyo. We thank Ryo Okuwaki for the useful discussions. We would like to thank Editage (www.editage.com) for English language editing.

Authors' information

Shunsuke TAKEMURA, <http://orcid.org/0000-0002-7511-3443> Earthquake Research Institute, the University of Tokyo, 1-1-1 Yayoi, Bunkyo-ku, Tokyo, 113-0032, Japan, shunsuke@eri.u-tokyo.ac.jp

Kazuo YOSHIMOTO, <https://orcid.org/0000-0003-2411-948X> Graduate School of Nanobioscience, Department of Material System Science, Yokohama City University, 22-2 Seto, Kanazawa-ku, Yokohama 236-0027, Japan, k_yoshi@yokohama-cu.ac.jp

Katsuhiko SHIOMI, <https://orcid.org/0000-0003-3566-0749> Earthquake and Tsunami Research Division, National Research Institute for Earth Science and Disaster Resilience, 3-1 Tennodai, Tsukuba, Ibaraki 305-0006, Japan, shiom@bosai.go.jp

References

1. Agata R (2020) Introduction of covariance components in slip inversion of geodetic data following a non-uniform spatial distribution and application to slip deficit rate estimation in the Nankai Trough subduction zone. *Geophys J Int* 221:1832–1844. <https://doi.org/10.1093/gji/ggaa116>
2. Baba S, Takemura S, Obara K, Noda A (2020) Slow earthquakes illuminating interplate coupling heterogeneities in subduction zones. *Geophys Res Lett.* <https://doi.org/10.1029/2020GL088089>
3. Bernardi F, Braunmiller J, Kradolfer U, Giardini D (2004) Automatic regional moment tensor inversion in the European-Mediterranean region. *Geophys J Int* 157:703–716. <https://doi.org/10.1111/j.1365-246X.2004.02215.x>
4. Boore DM (1999) Basin Waves on a Seafloor Recording of the 1990 Upland, California, Earthquake: Implications for Ground Motions from a Larger Earthquake. *Bull Seismol Soc Am* 89:317–324
5. Day SM, Graves R, Bielak J et al (2008) Model for Basin Effects on Long-Period Response Spectra in Southern California. *Earthq Spectra* 24:257–277. <https://doi.org/10.1193/1.2857545>
6. Ekström G, Nettles M, Dziewoński AM (2012) The global CMT project 2004–2010: Centroid-moment tensors for 13,017 earthquakes. *Phys Earth Planet Inter* 200–201:1–9. <https://doi.org/10.1016/j.pepi.2012.04.002>
7. Fukuyama E, Ishida M, Dreger DS, Kawai H (1998) Automated seismic moment tensor determination by using on-line broadband seismic waveforms. *Zisin* 51:149–156. https://doi.org/10.4294/zisin1948.51.1_149
8. Furumura M, Furumura T, Wen KL (2001) Numerical simulation of Love wave generation in the Ilan Basin, Taiwan, during the 1999 Chi-Chi earthquake. *Geophys Res Lett* 28:3385–3388. <https://doi.org/10.1029/2001GL013114>
9. Furumura T, Hayakawa T (2007) Anomalous propagation of long-period ground motions recorded in Tokyo during the 23 October 2004 Mw 6.6 Niigata-ken Chuetsu, Japan, earthquake. *Bull Seismol Soc Am* 97:863–880. <https://doi.org/10.1785/0120060166>
10. Furumura T, Hayakawa T, Nakamura M et al (2008) Development of long-period ground motions from the Nankai trough, Japan, earthquakes: Observations and computer simulation of the 1944 Tonankai (Mw 8.1) and the 2004 SE Off-Kii Peninsula (Mw 7.4) earthquakes. *Pure Appl Geophys* 165:585–607. <https://doi.org/10.1007/s00024-008-0318-8>

11. Gao H, Shen Y (2014) Upper mantle structure of the Cascades from full-wave ambient noise tomography: Evidence for 3D mantle upwelling in the back-arc. *Earth Planet Sci Lett* 390:222–233. <https://doi.org/10.1016/j.epsl.2014.01.012>
12. Gokhberg A, Fichtner A (2016) Full-waveform inversion on heterogeneous HPC systems. *Comput Geosci* 89:260–268. <https://doi.org/10.1016/j.cageo.2015.12.013>
13. Goldstein P, Snoker A (2005) SAC Availability for the IRIS Community. In: Inc. Institutions Seismol. Data Manag. Cent. Electron. Newsl. <https://ds.iris.edu/ds/newsletter/vol7/no1/193/sac-availability-for-the-iris-community/>
14. Gomberg J (2018) Cascadia Onshore-Offshore Site Response, Submarine Sediment Mobilization, and Earthquake Recurrence. *J Geophys Res Solid Earth* 123:1381–1404. <https://doi.org/10.1002/2017JB014985>
15. Guo Y, Koketsu K, Miyake H (2016) Propagation mechanism of long-period ground motions for offshore earthquakes along the nankai trough: Effects of the accretionary wedge. *Bull Seismol Soc Am* 106:1176–1197. <https://doi.org/10.1785/0120150315>
16. Headquarters for Earthquake Research Promotion (2017) National seismic hazard maps for Japan. https://www.jishin.go.jp/evaluation/seismic_hazard_map/shm_report/shm_report_2017/
17. Hejrani B, Tkalcic H (2020) Resolvability of the centroid-moment-tensors for shallow seismic sources and improvements from modelling high-frequency waveforms. *J Geophys Res Solid Earth*. <https://doi.org/10.1029/2020JB019643>
18. Hejrani B, Tkalcic H, Fichtner A (2017) Centroid moment tensor catalogue using a 3-D continental scale Earth model: Application to earthquakes in Papua New Guinea and the Solomon Islands. *J Geophys Res Solid Earth* 122:5517–5543. <https://doi.org/10.1002/2017JB014230>
19. Helffrich G, Wookey J, Bastow I (2013) The Seismic Analysis Code. Cambridge University Press, Cambridge
20. Helffrich GR (1997) How good are routinely determined focal mechanisms? Empirical statistics based on a comparison of Harvard, USGS and ERI moment tensors. *Geophys J Int* 131:741–750. <https://doi.org/10.1111/j.1365-246X.1997.tb06609.x>
21. Hirose F, Nakajima J, Hasegawa A (2008) Three-dimensional seismic velocity structure and configuration of the Philippine Sea slab in southwestern Japan estimated by double-difference tomography. *J Geophys Res Solid Earth* 113:1–26. <https://doi.org/10.1029/2007JB005274>
22. Ito A, Sugioka H, Obama K et al (2017a) Upper boundaries of the Pacific and Philippine Sea plates near the triple junction off the Boso Peninsula deduced from ocean-bottom seismic observations. *Earth Planets Sp* 69:30. <https://doi.org/10.1186/s40623-017-0608-4>
23. Ito A, Tonegawa T, Uchida N et al (2019) Configuration and structure of the Philippine Sea Plate off Boso, Japan: constraints on the shallow subduction kinematics, seismicity, and slow slip events. *Earth Planets Sp* 71:111. <https://doi.org/10.1186/s40623-019-1090-y>
24. Ito A, Yamamoto Y, Hino R et al (2017b) Tomographic image of crust and upper mantle off the Boso Peninsula using data from an ocean – bottom seismograph array. *Earth Planets Sp*.

<https://doi.org/10.1186/s40623-017-0703-6>

25. Iwaki A, Maeda T, Morikawa N et al (2018) Effects of random 3D upper crustal heterogeneity on long-period (≥ 1 s) ground-motion simulations. *Earth Planets Sp* 70:156. <https://doi.org/10.1186/s40623-018-0930-5>
26. Kanamori H, Brodsky EE (2004) The physics of earthquakes. *Reports Prog Phys* 67:1429–1496. <https://doi.org/10.1088/0034-4885/67/8/R03>
27. Kaneko Y, Ito Y, Chow B et al (2019) Ultra-long Duration of Seismic Ground Motion Arising From a Thick, Low-Velocity Sedimentary Wedge. *J Geophys Res Solid Earth* 124:10347–10359. <https://doi.org/10.1029/2019JB017795>
28. Kasahara K, Morita Y, Hirata N et al (2009) Development of the Metropolitan Seismic Observation network (MeSO-net) for Detection of Mega-thrust beneath Tokyo Metropolitan Area. *Bull Earthq Res Inst Univ Tokyo* 2:71–88
29. Kennett BLN, Fichtner A, Fishwick S, Yoshizawa K (2013) Australian seismological reference model (AuSREM): Mantle component. *Geophys J Int* 192:871–887. <https://doi.org/10.1093/gji/ggs065>
30. Kimura T, Murakami H, Matsumoto T (2015) Systematic monitoring of instrumentation health in high-density broadband seismic networks. *Earth Planets Sp* 67:55. <https://doi.org/10.1186/s40623-015-0226-y>
31. Kinoshita S, Fujiwara H, Mikoshiba T, Hoshino T (1992) Secondary Love waves observed by a strong-motion array in the Tokyo lowlands, Japan. *J Phys Earth* 40:99–116. <https://doi.org/10.4294/jpe1952.40.99>
32. Koketsu K, Kikuchi M (2000) Propagation of seismic ground motion in the Kanto basin, Japan. *Science* 288:1237–1239. <https://doi.org/10.1126/science.288.5469.1237>
33. Koketsu K, Miyake H (2008) A seismological overview of long-period ground motion. *J Seismol* 12:133–143. <https://doi.org/10.1007/s10950-007-9080-0>
34. Koketsu K, Miyake H, Afnimar, Tanaka Y (2009) A proposal for a standard procedure of modeling 3-D velocity structures and its application to the Tokyo metropolitan area, Japan. *Tectonophysics* 472:290–300. <https://doi.org/10.1016/j.tecto.2008.05.037>
35. Koketsu K, Miyake H, Suzuki H (2012) Japan Integrated Velocity Structure Model Version 1. *Proc 15th World Conf Earthq Eng* 1–4
36. Komatitsch D (2004) Simulations of Ground Motion in the Los Angeles Basin Based upon the Spectral-Element Method. *Bull Seismol Soc Am* 94:187–206. <https://doi.org/10.1785/0120030077>
37. Kubo A, Fukuyama E, Kawai H, Nonomura K (2002) NIED seismic moment tensor catalogue for regional earthquakes around Japan: Quality test and application. *Tectonophysics* 356:23–48. [https://doi.org/10.1016/S0040-1951\(02\)00375-X](https://doi.org/10.1016/S0040-1951(02)00375-X)
38. Kuge K, Kawakatsu H (1993) Significance of non-double couple components of deep and intermediate-depth earthquakes: implications from moment tensor inversions of long-period seismic waves. *Phys Earth Planet Inter* 75:243–266. [https://doi.org/10.1016/0031-9201\(93\)90004-S](https://doi.org/10.1016/0031-9201(93)90004-S)

39. Lee S-J, Liang WT, Cheng HW et al (2013) Towards real-time regional earthquake simulation I: Real-time moment tensor monitoring (RMT) for regional events in Taiwan. *Geophys J Int* 196:432–446. <https://doi.org/10.1093/gji/ggt371>
40. Maeda T, Takemura S, Furumura T (2017) OpenSWPC: an open-source integrated parallel simulation code for modeling seismic wave propagation in 3D heterogeneous viscoelastic media. *Earth Planets Sp* 69:102. <https://doi.org/10.1186/s40623-017-0687-2>
41. Miyake H, Koketsu K (2005) Long-period ground motions from a large offshore earthquake: The case of the 2004 off the Kii peninsula earthquake, Japan. *Earth Planets Sp* 57:203–207. <https://doi.org/10.1186/BF03351816>
42. Miyazawa M (2016) An investigation into the remote triggering of the Oita earthquake by the 2016 Mw 7.0 Kumamoto earthquake using full wavefield simulation. *Earth Planets Sp* 68:. <https://doi.org/10.1186/s40623-016-0585-z>
43. Miyoshi T, Obayashi M, Peter D et al (2017) Adjoint tomography of the crust and upper mantle structure beneath the Kanto region using broadband seismograms. *Prog Earth Planet Sci* 4:29. <https://doi.org/10.1186/s40645-017-0143-8>
44. Mukai Y, Furumura T, Maeda T (2018) Causes of Azimuthally Dependent Amplification Variations of Long-period Ground Motions in the Kanto Basin, Central Japan. *Bull Earthq Res Inst Univ Tokyo* 93:31–48
45. Nakamura T, Takenaka H, Okamoto T et al (2015) Long-period ocean-bottom motions in the source areas of large subduction earthquakes. *Sci Rep* 5:1–2. <https://doi.org/10.1038/srep16648>
46. National Research Institute for Earth Science and Disaster Resilience (2019) NIED F-net. Natl Res Inst Earth Sci Disaster Resil. <https://doi.org/10.17598/NIED.0005>
47. Oba A, Furumura T, Maeda T (2020) Data Assimilation-Based Early Forecasting of Long-Period Ground Motions for Large Earthquakes Along the Nankai Trough. *J Geophys Res Solid Earth* 125:. <https://doi.org/10.1029/2019JB019047>
48. Okada Y, Kasahara K, Hori S et al (2004) Recent progress of seismic observation networks in Japan –Hi-net, F-net, K-NET and KiK-net—. *Earth Planets Sp* 56:xv–xxviii. <https://doi.org/10.1186/BF03353076>
49. Okamoto T, Takenaka H, Nakamura T (2018) Evaluation of accuracy of synthetic waveforms for subduction-zone earthquakes by using a land–ocean unified 3D structure model. *Earth Planets Sp* 70:. <https://doi.org/10.1186/s40623-018-0871-z>
50. Olsen KB, Day SM, Minster JB et al (2006) Strong shaking in Los Angeles expected from southern San Andreas earthquake. *Geophys Res Lett* 33:L07305. <https://doi.org/10.1029/2005GL025472>
51. Sakai S, Hirata N (2009) Distribution of the Metropolitan Seismic Observation network. *Bull Earthq Res Inst Tokyo Univ* 84:57–69
52. Stephenson WJ, Reitman NG, Angster SJ (2017) P- and S-wave velocity models incorporating the Cascadia subduction zone for 3D earthquake ground motion simulations, Version 1.6—Update for Open-File Report 2007–1348

53. Takemura S, Akatsu M, Masuda K et al (2015) Long-period ground motions in a laterally inhomogeneous large sedimentary basin: observations and model simulations of long-period surface waves in the northern Kanto Basin, Japan. *Earth Planets Sp* 67:33. <https://doi.org/10.1186/s40623-015-0201-7>
54. Takemura S, Kimura T, Saito T et al (2018a) Moment tensor inversion of the 2016 southeast offshore Mie earthquake in the Tonankai region using a three-dimensional velocity structure model: effects of the accretionary prism and subducting oceanic plate. *Earth Planets Sp* 70:50. <https://doi.org/10.1186/s40623-018-0819-3>
55. Takemura S, Kubo H, Tonegawa T et al (2019a) Modeling of Long-Period Ground Motions in the Nankai Subduction Zone: Model Simulation Using the Accretionary Prism Derived from Oceanfloor Local S-Wave Velocity Structures. *Pure Appl Geophys* 176:627–647. <https://doi.org/10.1007/s00024-018-2013-8>
56. Takemura S, Matsuzawa T, Kimura T et al (2018b) Centroid Moment Tensor Inversion of Shallow Very Low Frequency Earthquakes Off the Kii Peninsula, Japan, Using a Three-Dimensional Velocity Structure Model. *Geophys Res Lett* 45:6450–6458. <https://doi.org/10.1029/2018GL078455>
57. Takemura S, Matsuzawa T, Noda A et al (2019b) Structural Characteristics of the Nankai Trough Shallow Plate Boundary Inferred From Shallow Very Low Frequency Earthquakes. *Geophys Res Lett* 46:4192–4201. <https://doi.org/10.1029/2019GL082448>
58. Takemura S, Okuwaki R, Kubota T et al (2020) Centroid moment tensor inversions of offshore earthquakes using a three-dimensional velocity structure model: slip distributions on the plate boundary along the Nankai Trough. *Geophys J Int* 222:1109–1125. <https://doi.org/10.1093/gji/ggaa238>
59. Takemura S, Shiomi K, Kimura T, Saito T (2016) Systematic difference between first-motion and waveform-inversion solutions for shallow offshore earthquakes due to a low-angle dipping slab. *Earth Planets Sp* 68:149. <https://doi.org/10.1186/s40623-016-0527-9>
60. Takemura S, Shiomi K, Obara K (2019c) 3D simulation of seismic wave propagation during the MJMA 6.3 Hyuga-nada earthquake occurred on 10 May 2019. *Rep Coord Comm Earthq Predict Japan* 102:320–325
61. Tape C, Liu Q, Maggi A, Tromp J (2009) Adjoint tomography of the southern California crust. *Science* 325:988–992. <https://doi.org/10.1126/science.1175298>
62. Vallée M, Charléty J, Ferreira AMG et al (2011) SCARDEC: A new technique for the rapid determination of seismic moment magnitude, focal mechanism and source time functions for large earthquakes using body-wave deconvolution. *Geophys J Int* 184:338–358. <https://doi.org/10.1111/j.1365-246X.2010.04836.x>
63. Wang X, Zhan Z (2020) Moving from 1-D to 3-D velocity model: automated waveform-based earthquake moment tensor inversion in the Los Angeles region. *Geophys J Int* 220:218–234. <https://doi.org/10.1093/gji/ggz435>

64. Wessel P, Smith WHF, Scharroo R et al (2013) Generic mapping tools: Improved version released. *Eos* (Washington DC) 94:409–410. <https://doi.org/10.1002/2013EO450001>
65. Wirth EA, Vidale JE, Frankel AD et al (2019) Source-Dependent Amplification of Earthquake Ground Motions in Deep Sedimentary Basins. *Geophys Res Lett* 46:6443–6450. <https://doi.org/10.1029/2019GL082474>
66. Yoshimoto K, Takemura S (2014) A study on the predominant period of long-period ground motions in the Kanto Basin, Japan. *Earth Planets Sp* 66:100. <https://doi.org/10.1186/1880-5981-66-100>

Figures

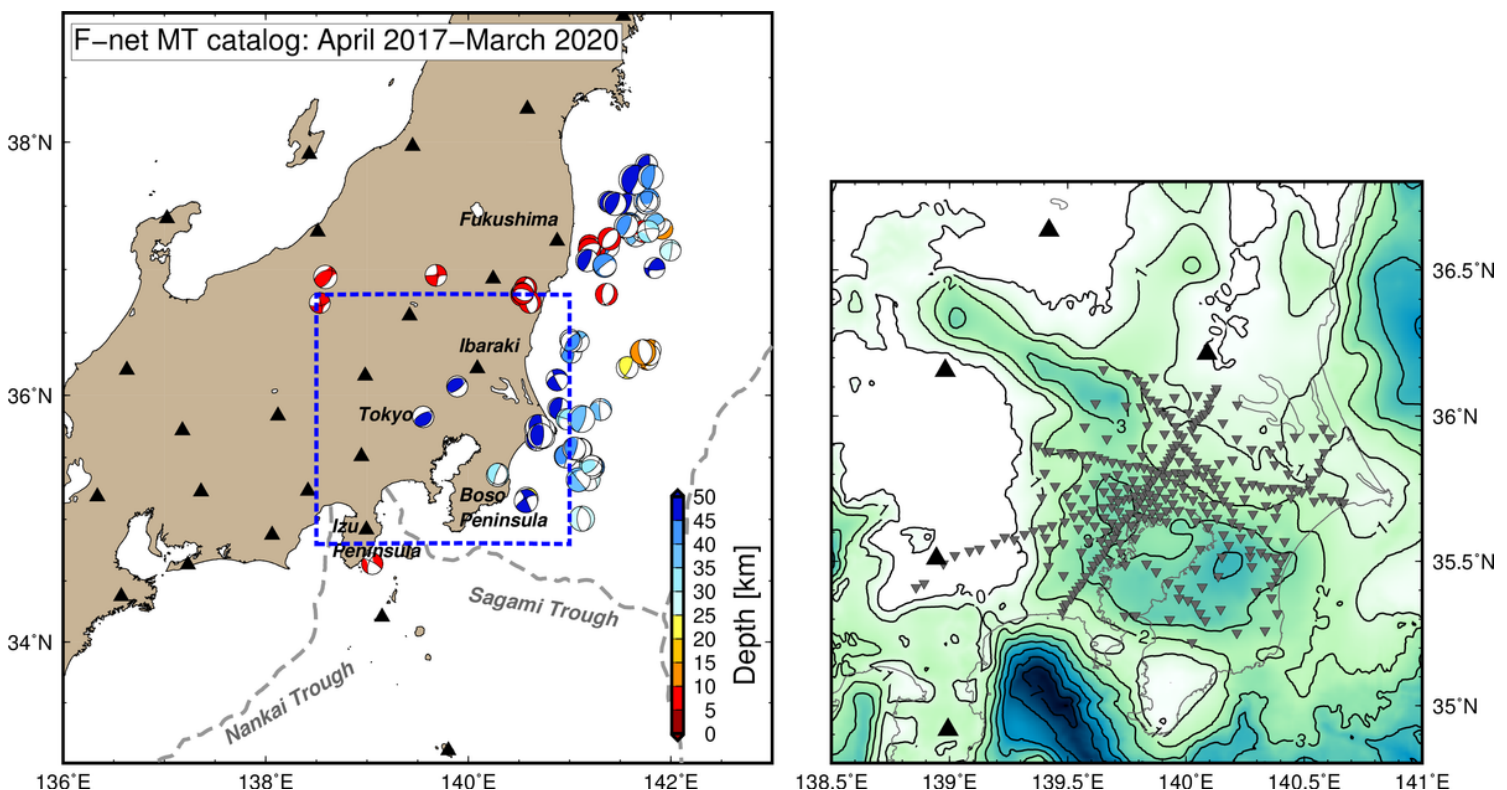


Figure 1

Map of the Kanto region, Japan. The filled black triangles are F-net stations. Plotted focal mechanisms are moment tensor (MT) solutions listed in the F-net MT catalog. The left panel is an enlarged map of the area enclosed by the blue dashed line. Inverse triangles in the left panel are MeSO-net stations.

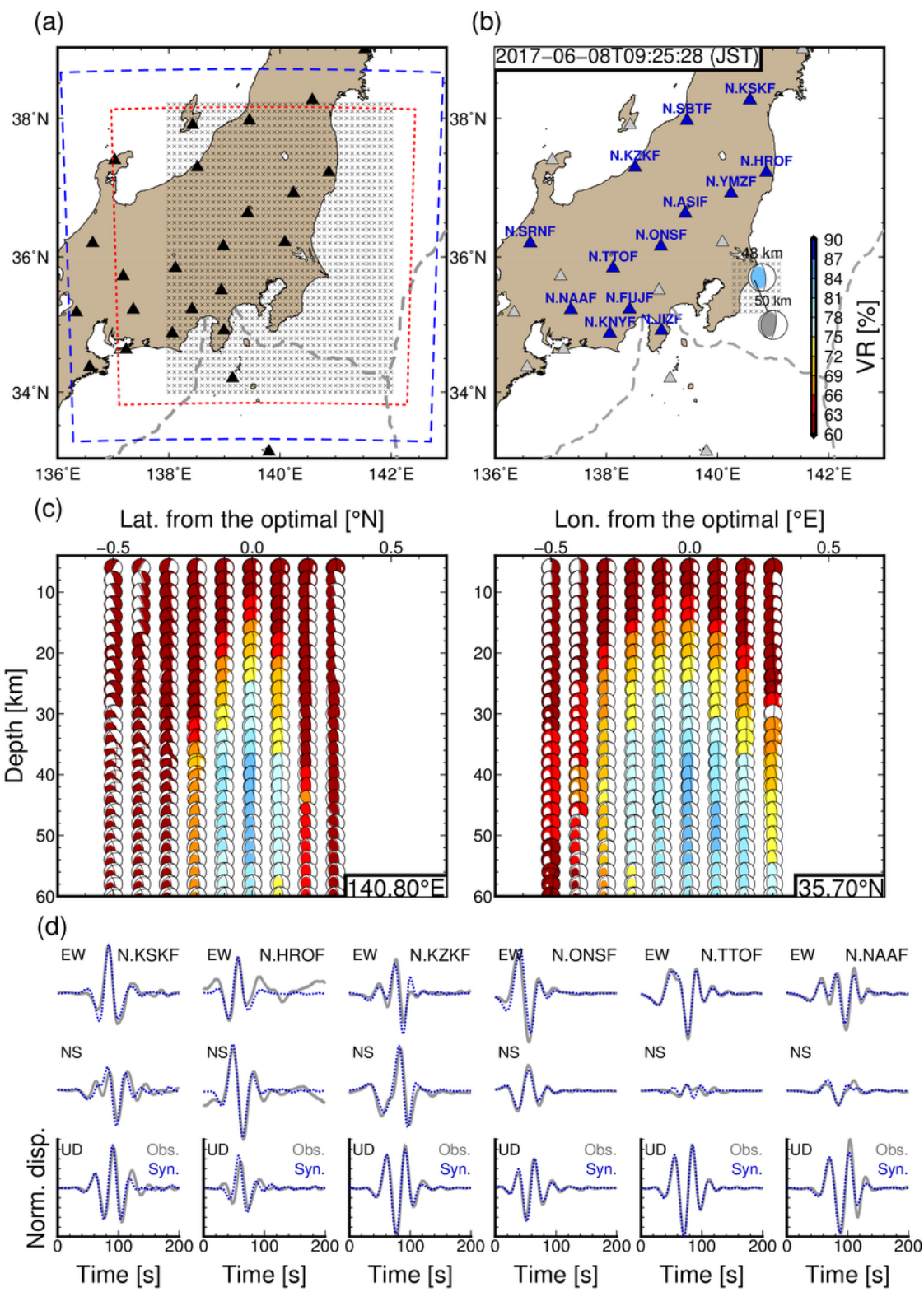


Figure 2

. Settings and an example of 3D CMT inversion in the Kanto region. (a) Simulation settings to evaluate Green's functions. The regions enclosed by the blue dashed and red dotted lines represent the horizontal coverage of the simulation model regions for evaluating Green's functions and long-period ground motion simulations, respectively. The triangles and crosses in the map denote the locations of the F-net stations and the assumed source grids, respectively. (b-d) an example of a CMT solution for an earthquake on

June 8, 2017, the location and depth of the optimal solution, used stations, and depth variations of optimal solutions at each source grid. Colors of the focal mechanisms reflect values of variance reduction between observed and synthetic displacements in the 25–100 s period band. The numbers above the optimal solutions in (b) are the optimal centroid depths. The grey focal mechanism in (b) is the F-net MT solution of this earthquake. The blue triangles in (b) are used F-net stations. (c) Spatial variations of VRs along latitude-depth and longitude-depth planes. (d) Examples of comparisons between observed and synthetic displacements in the 25–100 s period band. Gray solid and blue dotted lines are the observed and synthetic seismograms, respectively. Synthetic seismograms were evaluated by assuming the optimal solution. Amplitudes at each station were normalized by the maximum amplitude of observed and synthetic three-component displacement waveforms.

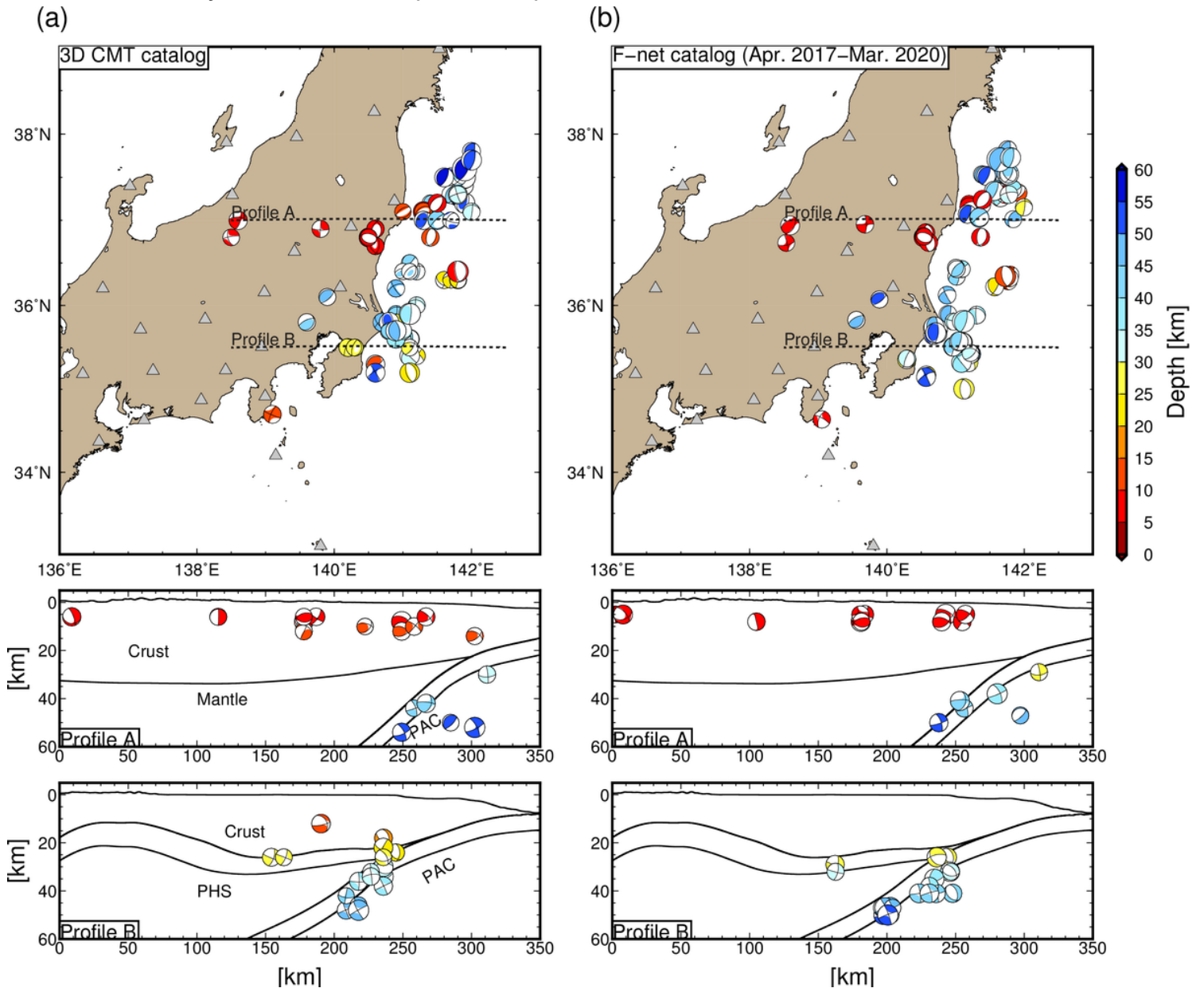


Figure 3

Results of 3D CMT inversion in the Kanto region. (a) 3D CMT catalog (this study), and (b) F-net MT catalog. Upper panels are map views of focal mechanisms. The colors represent the estimated centroid depth. The bottom panels show cross-sections along profiles A and B. In the bottom panels, topography, Moho, the upper surface of subducting plates, and the oceanic Moho are plotted.

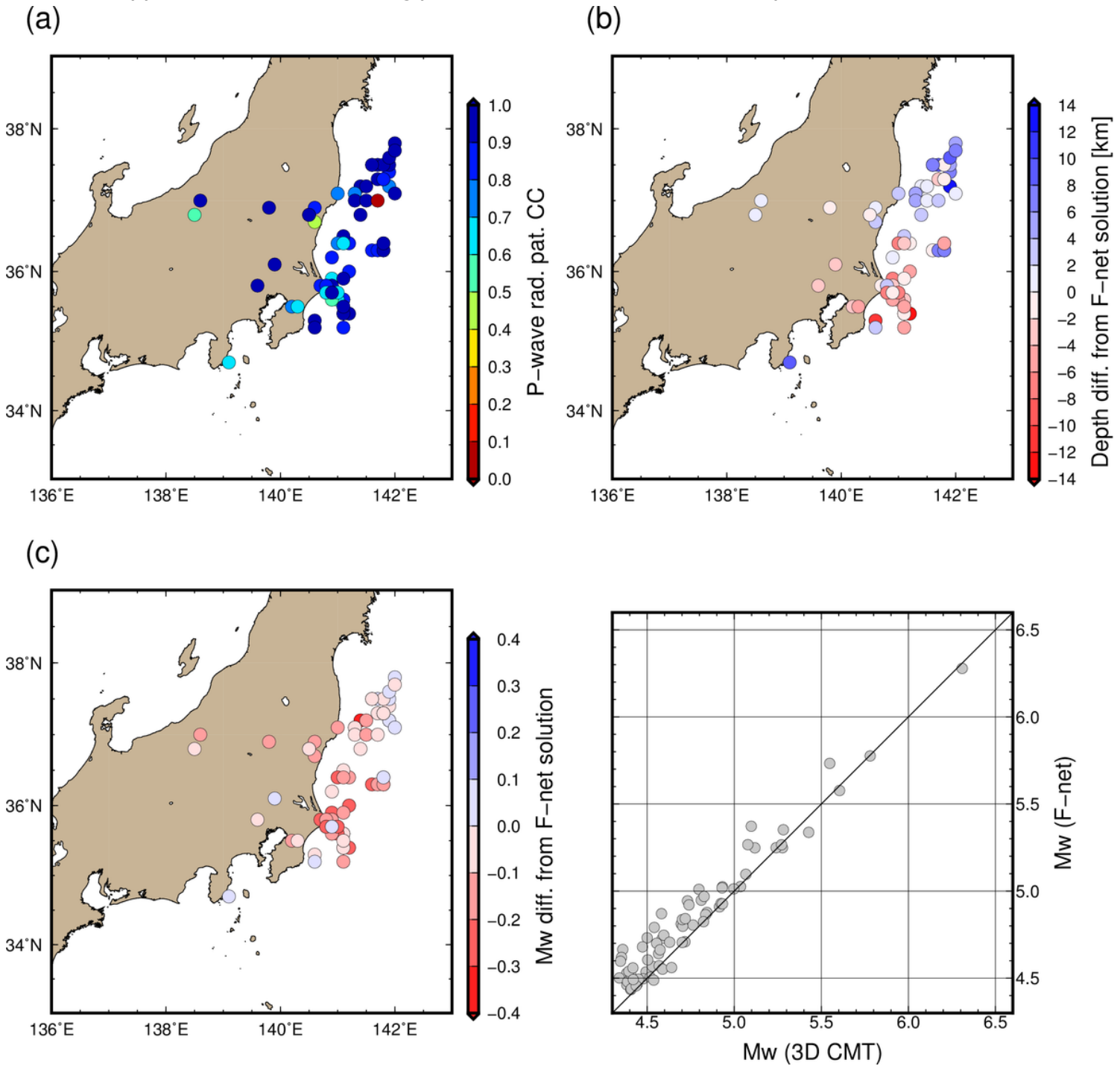


Figure 4

Differences between 3D CMT and F-net MT catalogs in the Kanto region. (a) Cross-correlation of P-wave radiation patterns (e.g., Kuge and Kawakatsu 1993; Helffrich 1997) between 3D CMT and F-net MT catalogs. (b) Depth differences and (c) Mw differences from F-net MT solutions.

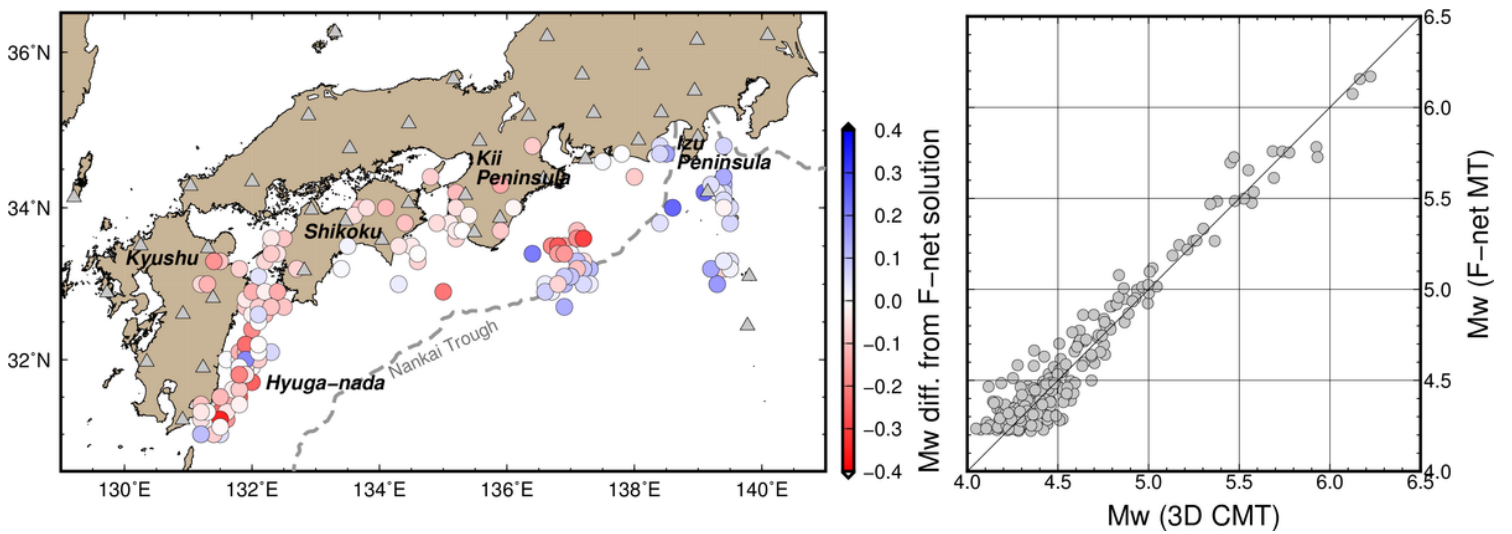
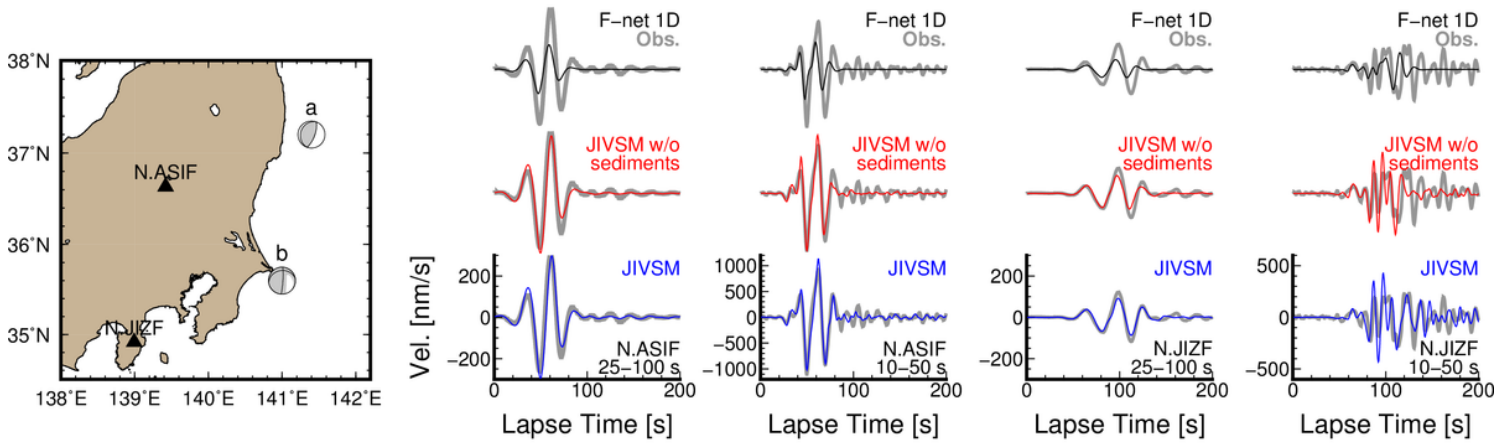


Figure 5

Differences in Mw values between F-net MT and 3D CMT solutions along the Nankai Trough. The 3D CMT catalog along the Nankai Trough was referred from Takemura et al. (2020).

(a)



(b)

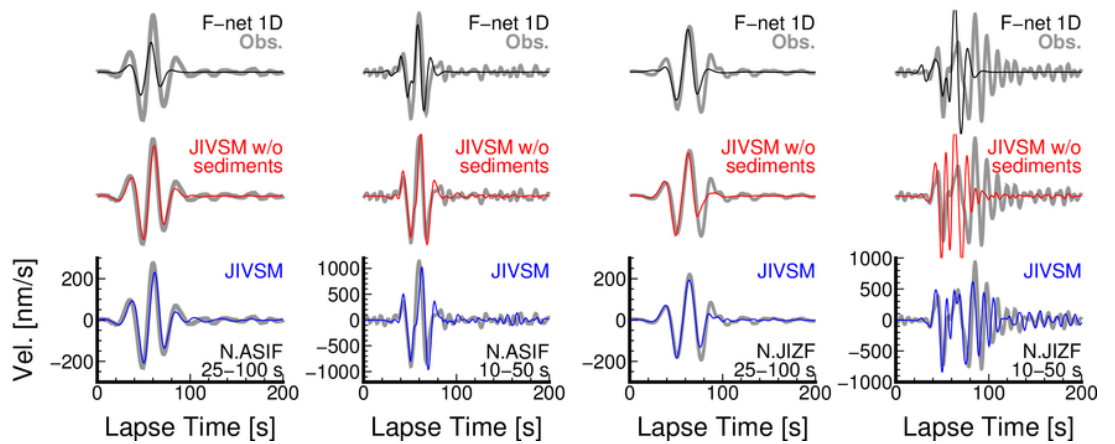


Figure 6

Simulations of long-period ground motion in various models. Simulation results of (a) Event a and (b) Event b. Observed F-net vertical seismograms are represented by bold gray lines. The black, red, and blue lines are simulated vertical seismograms of the JIVSM, JIVSM without sediments, and F-net 1D model, respectively. The physical parameters of sedimentary layers of the JIVSM without sediments were replaced with those of the upper crust (see Table 1). Locations of seismic sources and stations are illustrated in the upper left panel. Plotted focal mechanisms are the optimal solutions of events a and b.

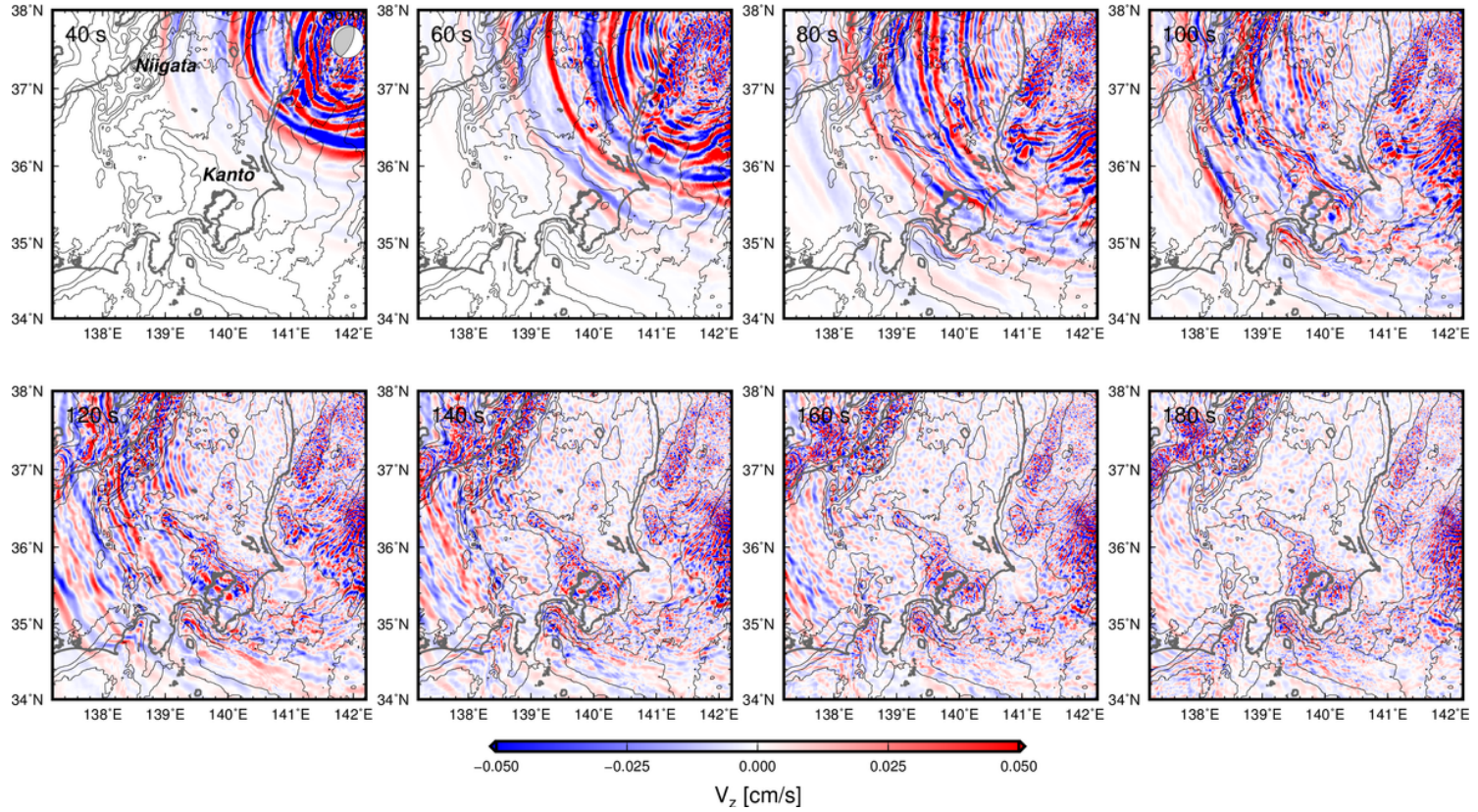


Figure 7

Snapshots of simulated vertical velocity wavefield for Event A. The numbers at the left-top corner are lapse times from the earthquake origin. The contour lines are the JIVSM bedrock depths at 2 km intervals.

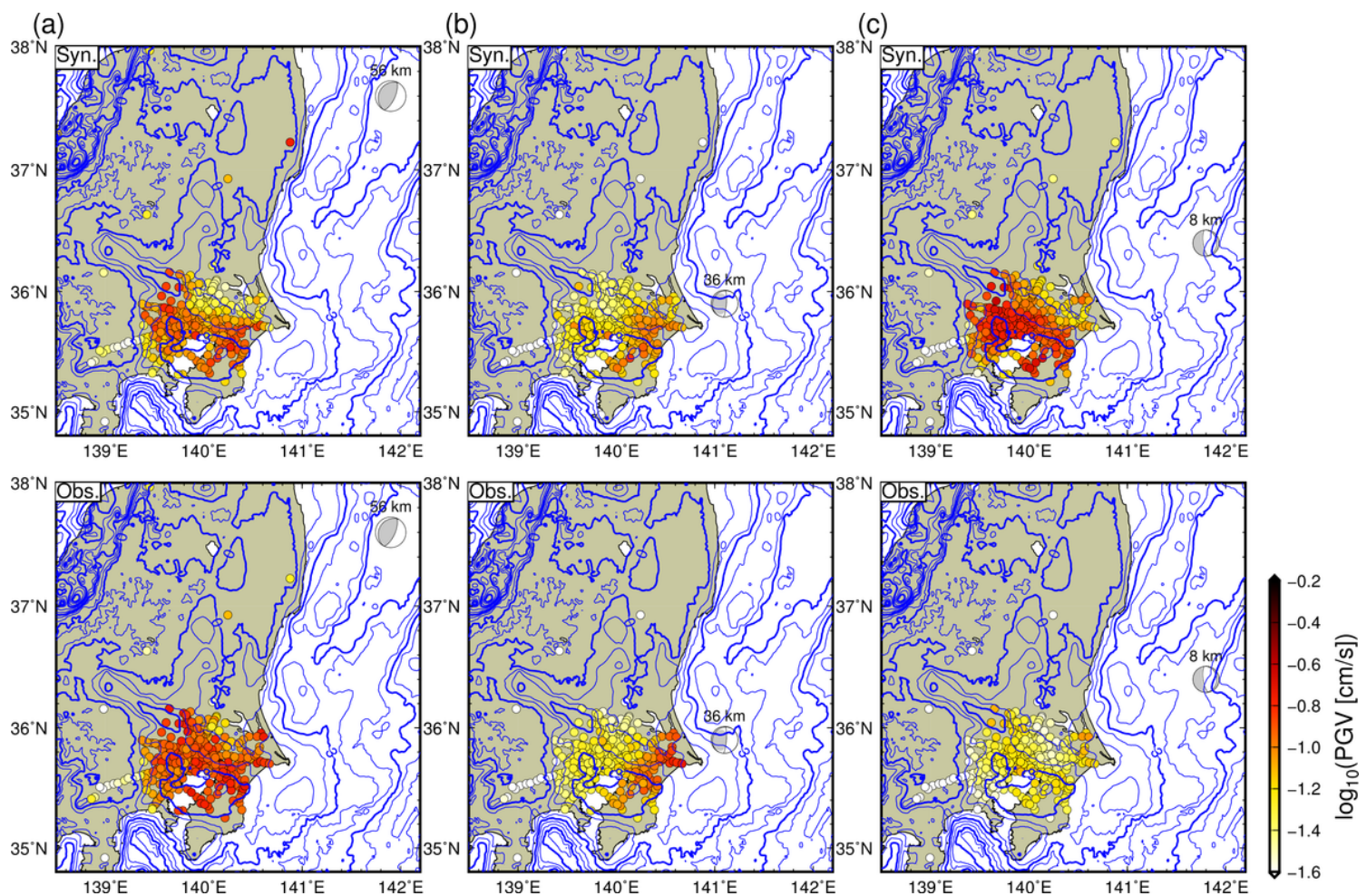


Figure 8

Peak ground velocity (PGV) for periods of 5–30 s. (a) Event A occurred on August 4, 2019, (b) Event B occurred on January 3, 2020, and (c) Event C occurred on February 6, 2020. Detail source parameters described in Events A–C of Table 3. The top and bottom panels are the synthetic and observed PGVs, respectively. PGVs were evaluated by calculating the vector sum of three-component filtered seismograms at the F-net and MeSO-net stations. Plotted focal mechanisms are the optimal solutions of the 3D CMT inversions for the corresponding events. The blue thin and bold contour lines are the JIVSM bedrock depths at 1.5 and 3 km intervals, respectively.

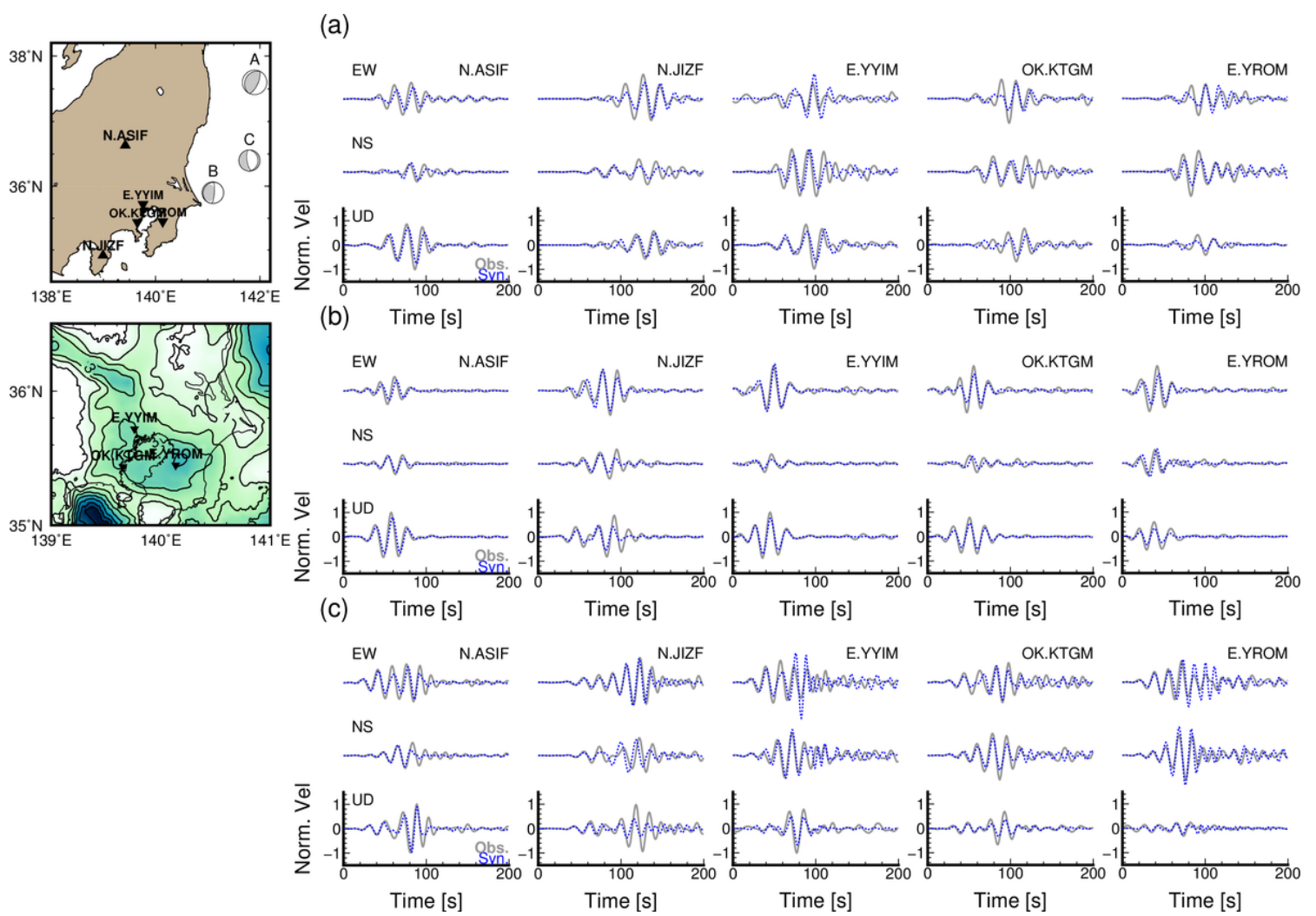


Figure 9

Comparisons between observed and simulated seismograms for periods of 15–30 s. We selected two F-net (N.ASIF and N.JIZF) and three MeSO-net (E.YYIM, OK.KTGM, and E.YROM) stations. Amplitudes at each station were normalized by the maximum amplitudes of observed seismograms for periods of 15–30 s at each station. (a) Event A, (b) Event B, and (c) Event C. Gray and blue dotted lines are the observed and simulated seismograms, respectively.

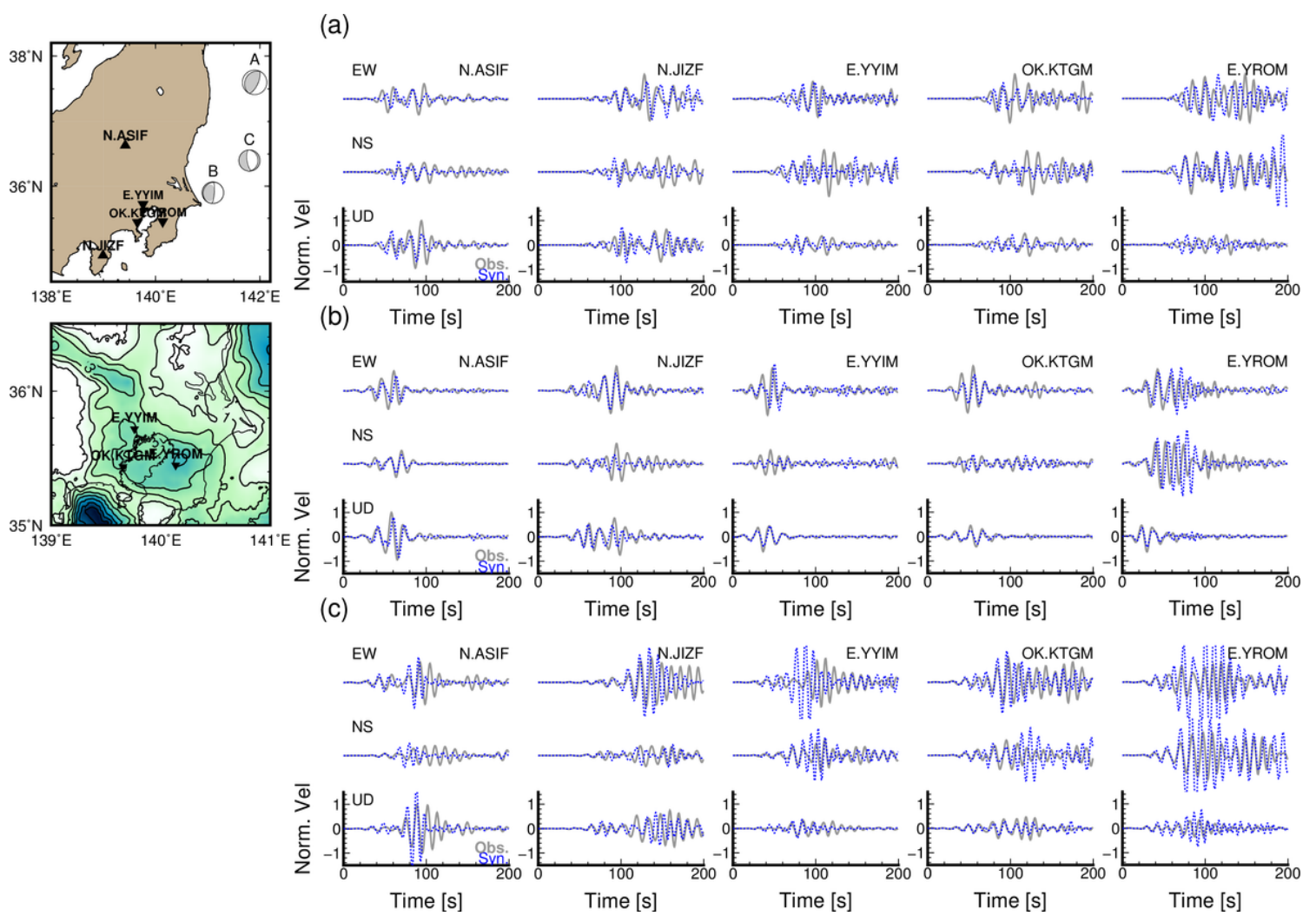


Figure 10

Comparisons between observed and simulated seismograms for periods of 10–20 s. We selected two F-net (N.ASIF and N.JIZF) and three MeSO-net (E.YYIM, OK.KTGM, and E.YROM) stations. Amplitudes at each station were normalized by the maximum amplitudes of observed seismograms for periods of 10–20 s at each station. (a) Event A, (b) Event B, and (c) Event C. Gray and blue dotted lines are the observed and simulated seismograms, respectively.

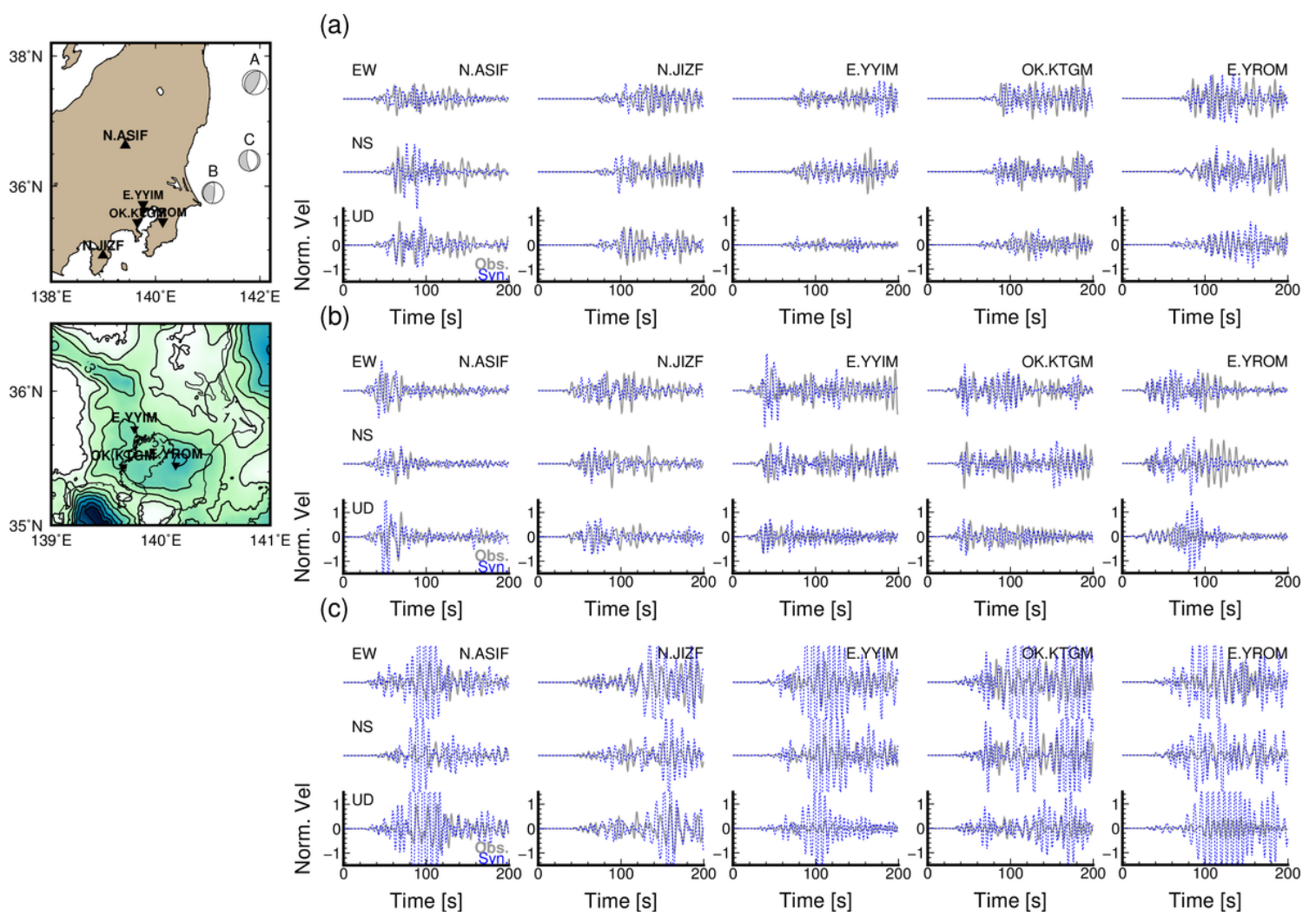


Figure 11

Comparisons between observed and simulated seismograms for periods of 5–16 s. We selected two F-net (N.ASIF and N.JIZF) and three MeSO-net (E.YYIM, OK.KTGM, and E.YROM) stations. Amplitudes at each station were normalized by the maximum amplitudes of observed seismograms for periods of 5–16 s at each station. (a) Event A, (b) Event B, and (c) Event C. Gray and blue dotted lines are the observed and simulated seismograms, respectively.

Supplementary Files

This is a list of supplementary files associated with this preprint. Click to download.

- Graphicalabstract.png